Nonlinear Elastic Buckling of Ultra-Thin Coilable Booms

Christophe Leclerc, Sergio Pellegrino*

Graduate Aerospace Laboratories
California Institute of Technology
1200 E. California Blvd, Pasadena, CA 91125, United States

Abstract

This paper presents a study of the elastic buckling behavior of Triangular Rollable And Collapsible (TRAC) booms under pure bending. An autoclave manufacturing process for ultra-thin composite booms is presented and the behavior of three test samples is investigated experimentally. Two regimes are observed, a pre-buckling regime and a stable post-buckling regime that ends when buckling collapse is reached. The buckling collapse moment, marking the end of the stable post-buckling regime, is typically four times higher than the initial buckling moment. A numerical simulation of the boom behavior with the Abaqus finite element package is presented and all of the features observed experimentally are captured accurately by the simulation, except buckling collapse. The numerical model is also used to study the effect of varying the boom length from 0.3 m to 5.0 m. It is shown that the pre-buckling deformation of the flanges under compression leads to a constant wavelength lateral-torsional buckling mode for which the critical moment is mostly constant across the range of lengths.

Keywords: Buckling, Thin-shell, Composite materials, Deployable boom, Space structure

1. Introduction

Deployable booms that can be flattened and coiled around a cylindrical hub are attractive for their packaging efficiency and their ability to deploy passively, by releasing the stored elastic strain energy. Coilable booms can be used to deploy large planar structures such as antennas (Leipold et al., 2005), photovoltaic surfaces (Campbell et al., 2006; Hoang et al., 2016) and solar sails (Leipold et al., 2003; Banik and Ardelean, 2010). The simplest example is the standard tape measure, but other designs such as the Storable Tubular Extendible Member (STEM) (Rimrott, 1965), the Collapsible Tube Mast (CTM) (Aguirre-Martinez

*Corresponding author. Email: sergiop@caltech.edu

et al., 1986; Herbeck et al., 2001), and the SHEARLESS boom (Fernandez, 2017, 2018) offer better mechanical performance.

A concept for coilable booms that is of particular interest to the present study is the Triangular Rollable And Collapsible (TRAC) boom (Murphey and Banik, 2011) invented by Murphey and Banik and developed by the Air Force Research Laboratory. The TRAC boom cross-section consists of two circular arcs (tape springs) attached along one edge, forming two curved flanges and a flat web, as shown in Figure 1. It has higher bending stiffness-to-packaged-height ratio than the CTM and the STEM booms (Roybal et al., 2007). Booms of this type have been flown on three different solar sails demonstrations, NASA's NanoSail-D (Whorton et al., 2008; Johnson et al., 2011), the Planetary Society's LightSail-1 (Biddy and Svitek, 2012) and LightSail-2 (Betts et al., 2017). In all three cases, the booms were made from a metal alloy. Recent research has shown that metallic TRAC booms are sensitive to thermal gradients, causing large tip deflections when one flange is facing the sun in space, while the other flange remains in the shadow (Stohlman and Loper, 2016). This has led to TRAC booms made of composite materials being studied extensively in recent years.

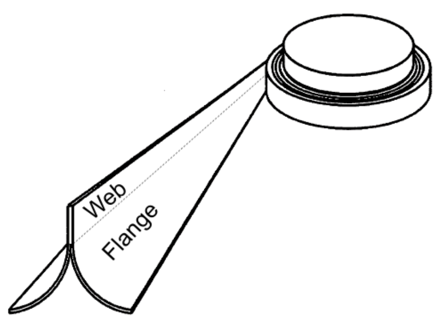

(a) TRAC boom partially coiled around a cylindrical hub (modified from Murphey and Banik (2011)).

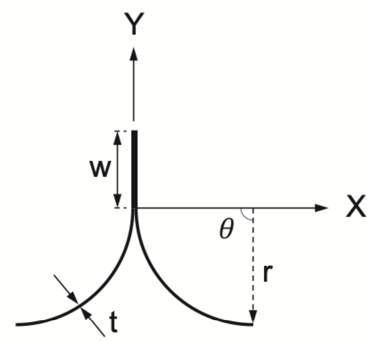

(b) TRAC boom cross-section.

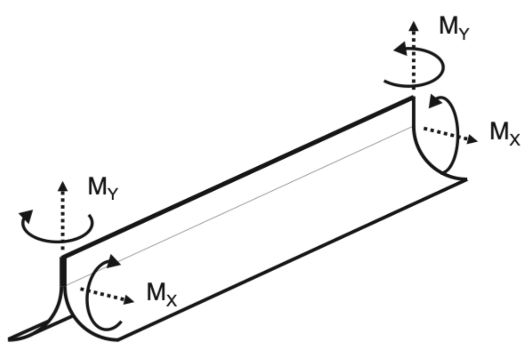

(c) Sign convention for positive bending moments.

Figure 1: TRAC boom architecture. The main geometric parameters are the flange radius r, thickness t and opening angle θ_f, the web width w, and the coiling radius R.

Due to its thin-walled open cross-section, the TRAC boom shows a complex, nonlinear behavior both in the deployed configuration and during coiling (Murphey et al., 2017). It has previously been shown that local buckling occurs during flattening and coiling of these booms, which can lead to material failure (Leclerc et al., 2018; Cox and Medina, 2019). Furthermore, localized buckling was observed to be the main structural failure mode for deployed booms under pure bending (Murphey et al., 2017; Leclerc et al., 2017). Banik and Murphey (2010) showed that nonlinear finite element analysis can accurately predict the bending behavior of booms that are relatively thick ($t \approx 1$ mm). Bessa and Pellegrino (2017) studied numerically the behavior of ultra-thin ($t < 100$ µm) TRAC booms under pure bending and presented an optimization of the cross-section that reduces the effect of shape imperfections on the moment for which the boom collapses. Both of these studies considered rather short booms, with lengths of 0.6 m and 0.5 m, respectively.

A recent system-level study of deployable space solar power satellites envisages simply supported structural elements with the TRAC cross-section and up to 60 m long, requiring a relatively small bending stiffness of around $5\,\mathrm{N\,m^2}$ (Arya et al., 2016). These structural elements are mainly loaded in bending. This study also showed that the packaging efficiency of these satellites increases significantly by reducing the flange thickness of the elements with TRAC cross section.

The present paper focuses on the performance of ultra-thin composite TRAC booms loaded in bending, aiming to study their buckling behavior under pure bending. This problem shares some similarities with pure bending of other types of thin-walled beams with open cross-section, and more particularly T-beams, where both local buckling of the web and lateral-torsional buckling modes have been observed (Corona and Ellison, 1997).

A TRAC cross-section meeting the stiffness requirement was previously designed by the present authors (Leclerc et al., 2017), with dimensions $r = 12.7$ mm, $\theta = 90°$ and $w = 8$ mm, and it was also found that a FlexLam-type laminate (Pollard and Murphey, 2006), consisting of glass fiber/carbon fiber composites with a total thickness of 80 µm significantly reduces stress concentrations during coiling and hence allows a more compact packaging (Leclerc and Pellegrino, 2019).

One challenge of studying structures made of ultra-thin composites is that their material properties and structural performance are closely related to the manufacturing process through which they are built. Therefore, the present study begins with extensive experimental work that addresses these aspects. Then, a numerical model is developed and validated by comparison to the experimental results on booms of laboratory scale. This model is used to predict the behavior of booms of different lengths.

The paper is organized as follows. Section 2 describes the manufacturing of ultra-thin TRAC booms, the characterization of their material properties, and the technique to measure the shape of the booms. The experimental setup and the results are also presented. Section 3 describes the finite element simulations to analyze the buckling of the booms. Section 4 compares the experiments with the numerical simulations and discusses the results. The effect of varying the boom length is then studied in Section 5. Section 6 concludes the paper.

2. Experimental Characterization

A detailed experimental study of the buckling of TRAC booms under pure bending was carried out. The first part of this section describes the manufacturing process used to fabricate the test samples. Then, the material characterization and the shape measurements of the samples are presented, followed by a description of the experimental procedure and the results obtained from the tests.

2.1. Sample fabrication

TRAC booms were manufactured from ultra-thin composite prepregs. The laminate stacking sequence was $[\pm 45_{GFPW}/0_{CF}/\pm 45_{GFPW}]$, where $GFPW$ represents the JPS E-glass fabric (style 1067, 31 gsm) glass fiber plain weave prepreg with Patz PMT-F4 epoxy resin, while CF represents a unidirectional Torayca T800 carbon fiber prepreg tape with North Thin Ply Technology Thin-Preg 120 EPHTg-402 epoxy resin (30 gsm). The total thickness of this 3-ply laminate is about 80 µm.

Manufacturing was done in an autoclave using a two-cure process. The flanges were cured separately and then bonded together in a second cure cycle. The main steps are illustrated in Figure 2. First, the laminate was draped over two U-shape aluminum molds (Fig. 2a) to form the two flanges. Both parts were vacuum bagged together and autoclave cured. Then, a single ply of glass fiber plain weave, oriented at $\pm 45°$ to the axis of the molds, was used to bond together the two flanges (Fig. 2b). This step forms a 7-ply web region with stacking sequence $[\pm 45_{GFPW}/0_{CF}/\pm 45_{3,GFPW}/0_{CF}/\pm 45_{GFPW}]$. The two molds were clamped together using a set of bolts in order to apply adequate consolidation pressure on the web region (Fig. 2c). As all the bolts are situated below the laminate, shims were added at the base of the mold to ensure an even pressure distribution over the web region. A second autoclave cure was then performed to cure the bonding ply. Finally, the part was removed from the molds (Fig. 2d), the excess material was trimmed, and the samples were cut to a length of 575 mm (Fig. 2e).

The mold geometry and the final cutting step were designed to achieve the nominal geometric parameters for the TRAC boom: $r = 12.7$ mm, $\theta = 90°$ and $w = 8$ mm. However, due to cure-related residual stresses, the mean flange radius and opening angle of the resulting booms varied, as detailed in Section 2.3. In the current study shape variations are not a concern, but in future a post-cure cycle could be used to partially release the residual stresses before demolding the booms.

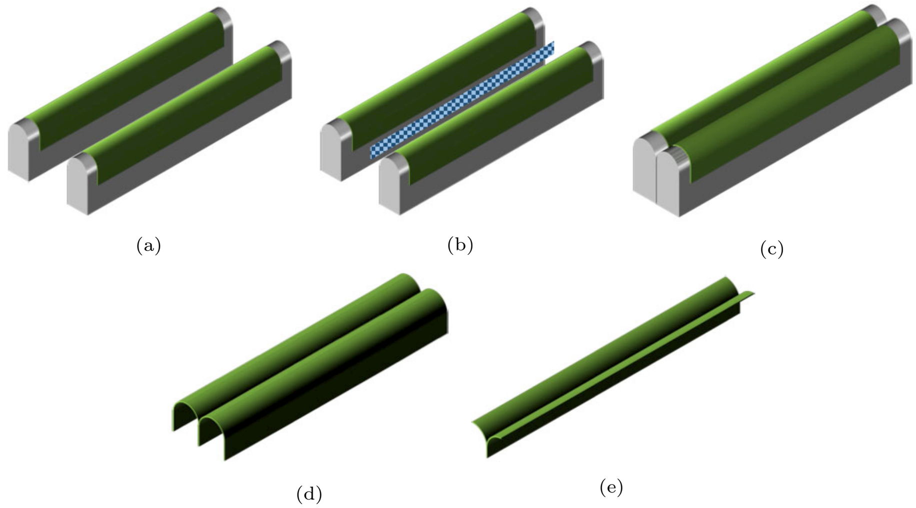

Figure 2: TRAC boom manufacturing process. Configuration for first cure, with two U-shape stacks shown in green (a), addition of bonding ply, shown in blue (b), configuration for second cure (c), cured part (d), and final structure (e).

2.2. Material characterization

E_1 and ν_{12} for the glass fiber plain weave, with the 1 and 2 directions aligned with the weave, were measured by performing tension tests on three 165 mm × 40 mm 4-ply flat laminate samples. The tensile force was measured with a 50 kN Instron load cell, while the axial and transverse strains between pairs of reflective tape strips attached to the samples were measured with two laser extensometers (LE-01 and LE-05 from Electronics Instrument Research). As the glass fabric has the same fiber count in the warp and weft directions, it was assumed that $E_1 = E_2$.

The shear modulus, G_{12}, was measured by performing 3-rail shear tests, as described in ASTM D4255/D4255M - 15a (2015). Three 151 mm × 138 mm samples were tested, with dimensions matching the Wyoming Test Fixtures CU-3R-6 used for these tests. The shear force was measured with a 50 kN Instron load cell, and the shear displacement with a laser extensometer.

The properties of the unidirectional carbon fiber prepregs had been previously measured by Ning and Pellegrino (2017). The properties of both materials are summarized in Table 1.

The elastic stiffness of the laminates was modeled with the $\boldsymbol{A}, \boldsymbol{D}$ matrices for symmetric laminates (Daniel and Ishai, 2005),

$$\begin{bmatrix} \boldsymbol{N} \\ \boldsymbol{M} \end{bmatrix} = \begin{bmatrix} \boldsymbol{A} & \boldsymbol{0} \\ \boldsymbol{0} & \boldsymbol{D} \end{bmatrix} \begin{bmatrix} \boldsymbol{\varepsilon^0} \\ \boldsymbol{\kappa} \end{bmatrix} \tag{1}$$

where $\boldsymbol{N}$ and $\boldsymbol{M}$ are the in-plane forces and out-of-plane moments per unit length, $\boldsymbol{\varepsilon^0}$ and $\boldsymbol{\kappa}$ are the mid-plane strains and curvatures, $\boldsymbol{A}$ is the in-plane stiffness matrix and $\boldsymbol{D}$ is the bending stiffness matrix.

The matrices $\boldsymbol{A}$ and $\boldsymbol{D}$ for the flange laminate were first calculated using the properties from Table 1, using classical lamination theory (CLT) (Daniel and Ishai, 2005). Tension and bending tests in both longitudinal and transverse directions were performed on flat samples of the flange laminate. From the tension tests, it was found that CLT had overestimated a_{11} by 13% and underestimated a_{22} by 15%, where the matrix $\boldsymbol{a}$ is the inverse of the $\boldsymbol{A}$ matrix. Therefore, these two elements of the $\boldsymbol{a}$ matrix were corrected accordingly and the $\boldsymbol{A}$ matrix was computed by inverting the corrected $\boldsymbol{a}$ matrix. D_{11} and D_{22} were measured by performing 4-point bending experiments. It was found that CLT had underestimated D_{11} and D_{22} by 8% and 6% respectively. Hence, the complete $\boldsymbol{D}$ matrix obtained from CLT was scaled up to correct the average error of 7%, as suggested in Sakovsky and Pellegrino (2019). In conclusion, the following flange laminate stiffness matrices were obtained:

$$\boldsymbol{A} = \begin{bmatrix} 5432 & 619 & 0 \\ 619 & 942 & 0 \\ 0 & 0 & 737 \end{bmatrix} N/mm \tag{2}$$

$$\boldsymbol{D} = \begin{bmatrix} 1.076 & 0.482 & 0 \\ 0.482 & 0.781 & 0 \\ 0 & 0 & 0.459 \end{bmatrix} Nmm \tag{3}$$

For the web laminate, CLT was used to estimate the $\boldsymbol{A}$ and $\boldsymbol{D}$ matrices. The $\boldsymbol{A}$ matrix was scaled in the same way as the flange laminate, increasing A_{11} by 14% and decreasing A_{22} by 13%. The $\boldsymbol{D}$ matrix was left unchanged. The stiffness matrices for the web were therefore:

$$\boldsymbol{A} = \begin{bmatrix} 11369 & 1512 & 0 \\ 1512 & 2269 & 0 \\ 0 & 0 & 1727 \end{bmatrix} N/mm \tag{4}$$

$$\boldsymbol{D} = \begin{bmatrix} 28.20 & 4.32 & 0 \\ 4.32 & 7.44 & 0 \\ 0 & 0 & 4.93 \end{bmatrix} Nmm \tag{5}$$

Table 1: Elastic properties of carbon fiber and glass fiber plain weave prepregs.

	E_1 [GPa]	E_2 [GPa]	G_{12} [GPa]	ν_{12}	t [µm]
CF	128	6.5	7.6	0.35	30
GFPW	23.8	23.8	3.3	0.17	25

2.3. TRAC boom shape characterization

Measurements of the actual shape of the three boom samples were made using a FaroArm Edge 14000 with a 3D laser scanner ScanArm HD attachment. A Matlab script was created to extract the cross-section geometry (flange radius and opening angle) at 10 locations along the length of each boom from the point cloud generated by the FaroArm. The script also estimated the twist angle along the length and the camber of the boom, defined as the distance between the centroid of the cross-section at each location and a straight line connecting the end centroids. The average cross-section geometric properties for the three samples obtained in this way are presented in Table 2. The specific geometry of each test sample was used in the simulation of each specific test.

Table 2: Nominal and average measured cross-section geometry for 575 mm long TRAC boom samples.

	r [mm]	θ_f [°]	w [mm]	Twist [°]	Camber [mm]
Nominal	12.7	90	8	0	0
Sample 1	11.8	91.3	8	10	0.8
Sample 2	11.9	88.5	8	9	1.0
Sample 3	11.5	95.7	8	7	0.4

2.4. Bending tests

The test setup for the bending experiments is shown in Figure 3. The samples were potted at each end with epoxy into flat acrylic plates with laser-cut thin slits matching the cross-section of each specific test sample. This ensured that the cross-section of the thin-shell booms was not distorted near the ends prior to testing.

The test setup allowed independent control of the rotation at each end, by means of hand-operated worm drives. The longitudinal translation of one end was not constrained, allowing the distance between the two ends to shorten in order to allow large bending deformations of the boom. A calibrated camera above the setup provided tracking of four targets installed on two rigid rods, to magnify the rotation at each end. The rotations were measured from the images using a Matlab script. The sample was mounted on hollow aluminum shafts instrumented with strain gauges to measure the moment at each end using a Vishay P3 strain amplifier. The resolution of the moment measurements was 0.009 Nm.

To perform a bending test, the end rotations were manually increased in small steps, keeping the moments equal in order to ensure a pure moment loading. Each step increased the applied moment by 0.018 Nm, and the readings at both ends were equal within the resolution of the measurement. Once the buckling collapse condition had been reached, the measured moments dropped significantly, and became different between the two ends. This condition indicated that the sample had buckled asymmetrically and was no longer loaded under pure bending.

Each sample was tested in bending around both axes, X and Y (defined in Figure 1). In the case of bending around X, the TRAC cross-section is not symmetric. Positive moments cause the web to be in compression, while

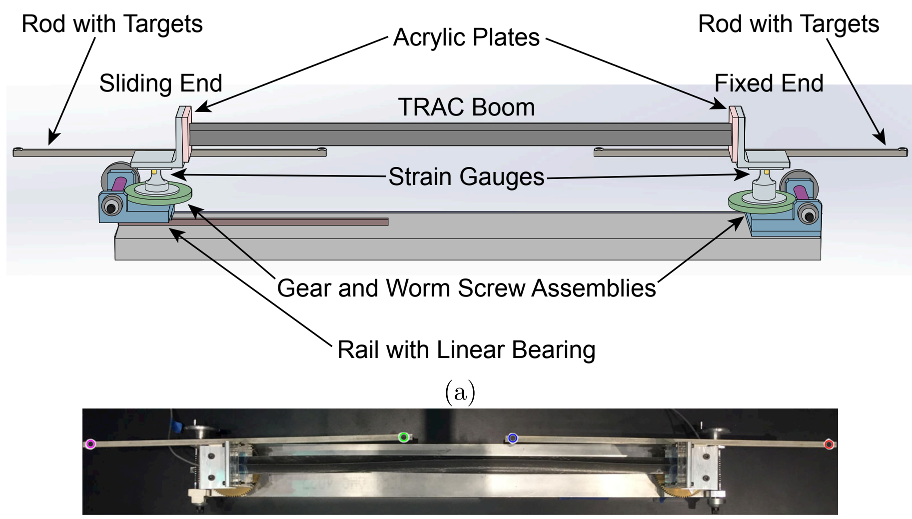

(a)

(b)

Figure 3: (a) Sketch of bending experimental setup. The sliding end is mounted on a linear bearing that allows longitudinal translation. (b) Top view of test setup showing a sample with long-wave buckling of web.

negative moments cause it to be in tension. Bending around Y is nominally symmetric.

2.5. Experimental results

The three test booms behaved consistently (although each boom behaves a bit differently, due its own unique geometry) and therefore only the results for the first boom are presented herein. Bending tests were performed three times in each of the four directions (both positive and negative moments M_X, M_Y) up to buckling collapse. In all cases, two regimes were observed. The first regime is a linear pre-buckling phase that lasts until the first buckling event. The corresponding moment is referred to as the critical moment. The second regime, following the initial buckling event, is a stable post-buckling phase that lasts until the buckling collapse. A loading-unloading test was also performed for each axis of bending, without reaching buckling collapse. For this test, the bending moment was increased starting from zero until one step before buckling collapse. Then, the moment was decreased to zero using the same step size. This loading-unloading cycle was performed for both signs of the moment. This result indicates that the behavior of the booms is fully reversible up to the buckling collapse, i.e. well beyond the critical moment.

The experimental results are shown in Figures 4 and 5. These plots show the measured moment as a function of the total rotation angle. The experiments were repeated three times and the measured behavior was practically indistinguishable, with an average variation of the angle for a given moment of 0.04°.

More importantly, the same buckling events (as described in the next paragraphs) were observed at the same loads and locations. Also, the results from the loading-unloading cycles show that the structural behavior of the booms is fully reversible even in the stable post-buckling regime.

Under moments M_X the overall deviation in the buckling collapse moment was 5%. Furthermore, the behavior was consistent between loading and unloading. Deviation between loading and unloading was only observed when a negative moment close to the collapse value was applied. Under moments M_Y the deviation in buckling collapse moments was 10%. In the case of negative moments, tests 2 and 3 captured some unstable behavior at rotations larger than 3°, while test 1 directly reached buckling collapse. Practically no difference was observed between loading and unloading.

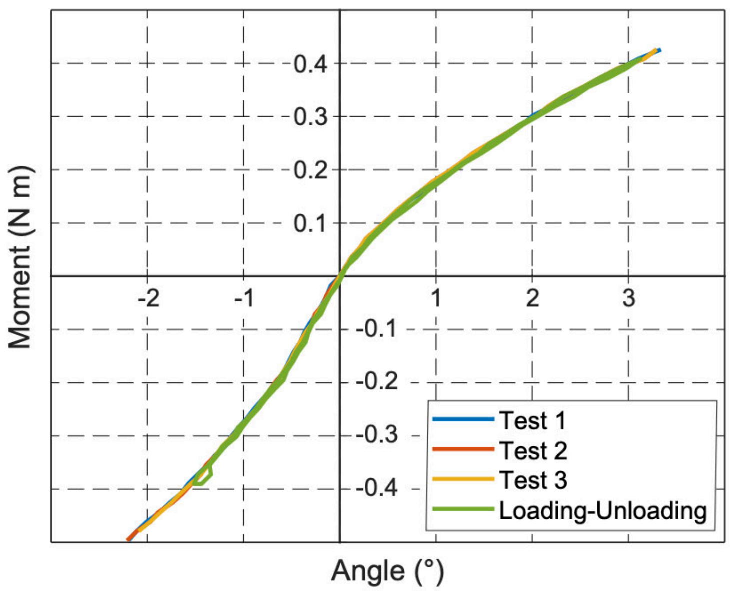

Figure 4: Measured moment vs. rotation results for sample 1 under moments M_X.

Figure 6 shows photos of the buckling modes during an experiment in which a moment M_X was applied. The web is under compression for $M_X > 0$. Beyond the critical moment (about 0.1 N m), the web starts to buckle globally in a wave pattern, with a wavelength of 1/4 of the total length. This reduces the effective stiffness of the boom and a softening of about 45% is observed in the moment-angle plot. Subsequently increasing the moment increases the amplitude of the web waviness, until the deformation localizes (always at the same location, 90 mm from the fixed end) and buckling collapse is reached. The maximum moment for this load case is 0.43 N m. Overall, two regimes were observed: pre-buckling, followed by a first buckling event, and stable post-buckling, followed by buckling collapse.

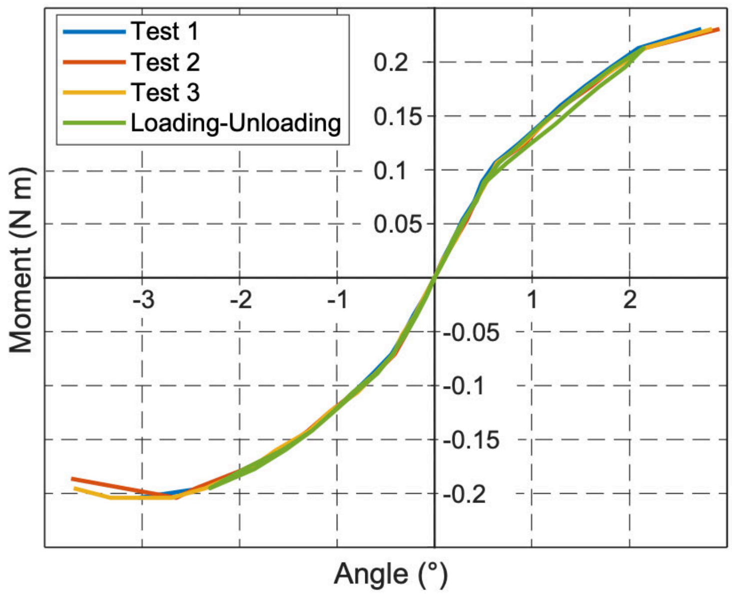

Figure 5: Measured moment vs. rotation results for sample 1 under moments M_Y.

The behavior of the boom loaded by a moment $M_X < 0$ has the same two regimes, but is different otherwise as in this case the flanges are under compression. At a critical moment of about $-0.21\,\mathrm{N\,m}$, a small localized buckle appears in one flange, quickly followed by a buckle in the other flange. These buckles lead to a softening of about 40%, as shown in Figure 6. At a load of $-0.4\,\mathrm{N\,m}$, the buckle in one flange moves longitudinally 20 mm towards the closest end of the boom. However, this displacement occurs at a different load (about $-0.35\,\mathrm{N\,m}$) during unloading, explaining the difference between loading and unloading observed in Figure 4. Buckling collapse occurs when a torsional instability forces one buckle to flatten transversally and form a kink at the junction of the flange with the web. The maximum moment for this load case is $-0.5\,\mathrm{N\,m}$.

Figure 7 shows the observed buckling modes when the boom was loaded by a moment M_Y. As the behavior is nominally symmetric, only the behavior under positive moments will be discussed. Since the inner flange is under compression, the buckling modes are similar to the case $M_X < 0$. First, there is a mostly linear pre-buckling regime. Then, at a critical moment of about $0.1\,\mathrm{N\,m}$, a small localized buckle appears in the compression flange, which reduces the effective stiffness of the boom by about 60%. In the stable post-buckling regime that follows, the buckle slowly increases in amplitude until the flange flattens and forms a kink at the root of the web. Buckling collapse occurs at a load of $0.23\,\mathrm{N\,m}$, due to a large buckle at a distance of 180 mm from the sliding end of the boom. Comparing Figures 6 and 7, the buckling collapse mode for

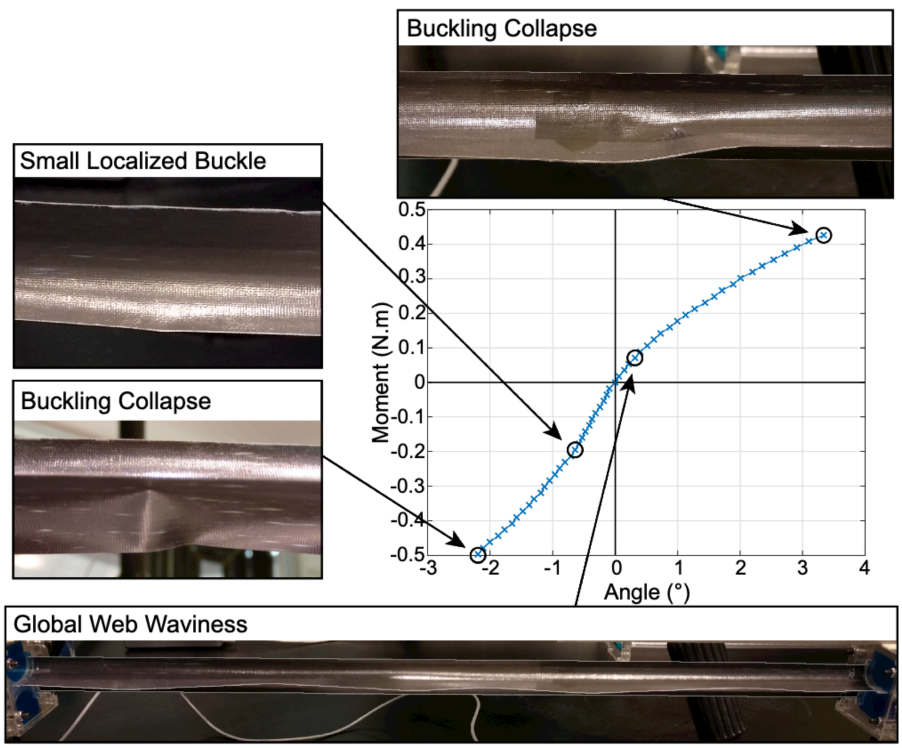

Figure 6: Buckling modes for positive and negative moments M_X.

moments M_Y of any sign is practically identical to the buckling collapse mode for moments $M_X < 0$.

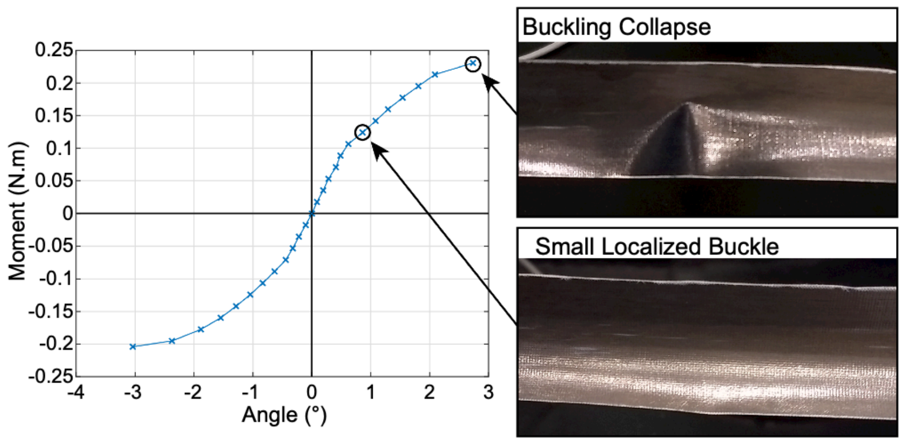

Figure 7: Buckling modes for moments $M_Y > 0$.

In summary, the initial buckling of ultra-thin TRAC booms under pure bending loading occurs when small localized buckles first appear, reducing the effective bending stiffness. This instability is followed by a stable post-buckling regime, where the structure is able to withstand moments up to four times higher than the initial buckling moment. In both of these regimes there is almost no difference between loading and unloading behavior, showing that the structural behavior is fully reversible up to the point of buckling collapse. Therefore, there is no residual deformation when a boom that has previously entered the stable post-buckling range is unloaded and then re-loaded. This is a useful result for applications involving cyclic loading.

3. Finite Element Simulations

The finite element model shown in Figure 8 was built in Abaqus/Standard 2018, to predict and study the detailed behavior of ultra-thin TRAC booms loaded by pure moments. The boom is modeled using 4-node shell elements with reduced integration (S4R). The finite element mesh is uniform, with element size of 2 mm corresponding to 20 elements across each flange and 4 elements across the web.

The material properties were defined through the $\boldsymbol{ABD}$ stiffness matrices given in Section 2.2.

The nodes forming the two end cross-sections were kinematically coupled to two reference points, in effect creating rigid cross-sections that match the end conditions of the experimental setup. All six degrees of freedom of the reference point at end 1 were constrained, defining a clamped condition. At the other

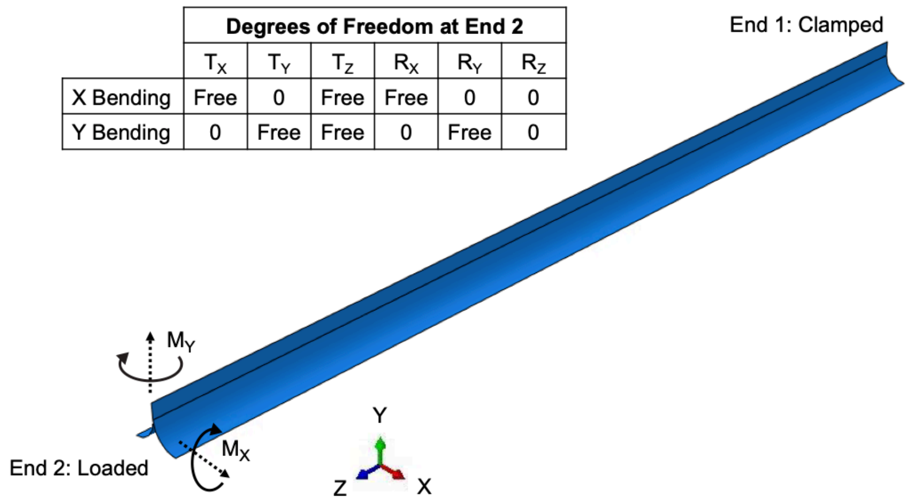

	Degrees of Freedom at End 2					
	T_X	T_Y	T_Z	R_X	R_Y	R_Z
X Bending	Free	0	Free	Free	0	0
Y Bending	0	Free	Free	0	Free	0

Figure 8: Finite element model with boundary conditions (T = translation, R = rotation) and applied moments.

end, a pure moment load was applied at the reference point. In the case of a moment M_X, the translational degrees of freedom along Y and Z as well as the rotational degree of freedom around X were left free, while the other three degrees of freedom were fixed. In the case of moments M_Y, the same boundary conditions were used, only inverting X and Y.

While these boundary conditions do not match the kinematics of the experimental setup, in both analysis and experiment the loading condition on the boom is that of a pure moment. Therefore, the two loading conditions are statically equivalent. A comparison was made between the model described above and a different model that matches exactly the boundary conditions of the experiments, and it was observed that they both predict the same buckling load. For this reason, the simpler model, where the applied moment and the resulting rotation are extracted at a single point, was chosen.

The analysis procedure consists of 4 steps and is similar to Bessa and Pellegrino (2017):

1. A preliminary buckling prediction (eigenvalue calculation) is performed starting from the undeformed configuration (*linear buckling prediction*).
2. An implicit, nonlinear static analysis is then performed, starting from the undeformed configuration until buckling occurs, at which point the analysis does not converge. This buckling load can be lower or higher than the previous, linear prediction. The goal of this step is to compute the deformed geometry just before buckling.
3. Next, a new linear buckling prediction is performed in the deformed configuration, using the results from the previous step. An iterative process is used to find the last increment at which the buckling prediction can

be obtained, as the nonlinear analysis will sometime converge for a few additional increments in the post-buckling regime. To achieve this, the applied load in the nonlinear static analysis is reduced until a linear buckling analysis can be performed successfully in the deformed configuration. The outcome of this analysis is a new prediction of the buckling load (*nonlinear buckling prediction*).

4. A simulation of the post-buckling regime is performed using an arc-length method (modified Riks method (Crisfield, 1981)), by introducing an initial geometric imperfection based on the first buckling mode found in step 3. For this study, an amplitude of 20% of the flange thickness (16 μm) was sufficient to trigger the post-buckling regime without changing the pre-buckling behavior.

Therefore, two buckling predictions are obtained from this analysis. The linear prediction is strictly from the undeformed configuration and does not account for geometric deformations, while the nonlinear prediction is obtained in the deformed configuration, and thus accounts for geometric nonlinearity in the prebuckling regime.

As in the experiments, three loading conditions were studied numerically. Figure 9 shows the different buckling modes obtained from the linear and nonlinear buckling predictions, as well as the post-buckling analysis, for each loading condition of a boom with the nominal cross-section and a length of 500 mm. A careful study of Fig. 9 leads to several interesting observations.

First, when a moment $M_X > 0$ is applied (web under compression), both the linear (fig. 9a) and nonlinear (fig. 9b) buckling involve a global wave pattern in the web, and the wave patterns in the two cases are in close agreement. In the post-buckling regime (fig. 9c) the buckling mode becomes localized.

Second, when a moment $M_X < 0$ is applied (flanges under compression), the linear buckling analysis (fig. 9d) predicts a global wave pattern for both flanges. The nonlinear analysis (fig. 9e) predicts localized buckles close to the two ends, whereas the post-buckling deformation (fig. 9f) has two kinks in each flange, close to the ends.

Third, in the case of a moment moment M_Y the linear buckling prediction (fig. 9g) is a global wave pattern on the flange loaded in compression, whereas for nonlinear buckling (fig. 9h) the buckling mode is localized in the middle. In the post-buckling regime (fig. 9i), a kink forms in the middle of the boom.

4. Comparison with Experiments

To assess the ability of the numerical model to closely predict the nonlinear buckling behavior of actual TRAC booms, simulations of specific experiments were carried out. Each simulation was set up with the cross-section of the finite element model matching the cross-section of the specific test sample, using the measured dimensions in Table 2. Since the agreement between experiments and their respective simulations was similar, only results for sample 1 are presented here.

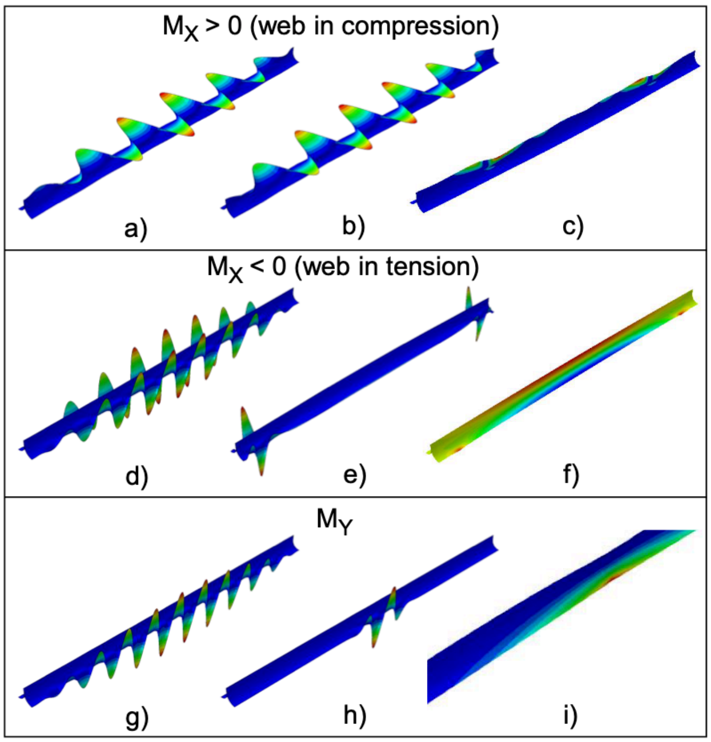

Figure 9: Buckling modes from three types of finite element simulations, for three load cases. $M_X > 0$: linear buckling (a), nonlinear buckling (b), post-buckling (c). $M_X < 0$: linear buckling (d), nonlinear buckling (e), post-buckling (f). M_Y linear buckling (g), nonlinear buckling (h), post-buckling (i). Contours show displacement magnitude.

Figure 10 shows the moment-angle plot for bending around X. For negative moments (web in tension), the simulations did not converge in the post-buckling regime. However, the initial buckling load from the simulation ($-0.25\,\mathrm{N\,m}$) is close to the first appearance of small localized buckles in the experiment ($-0.21\,\mathrm{N\,m}$). For positive moments (web in compression), the stable post-buckling regime is very well captured in the simulation. The softening observed in the experiments, due to the web undergoing global buckling, is also seen in the numerical results. Furthermore, the buckling collapse from the simulation ($0.5\,\mathrm{N\,m}$) is close to the experimental value ($0.43\,\mathrm{N\,m}$). The main difference between these two results is that while the simulation shows a clear transition from the pre-buckling regime to the post-buckling regime, this transition is more gradual in the experiments.

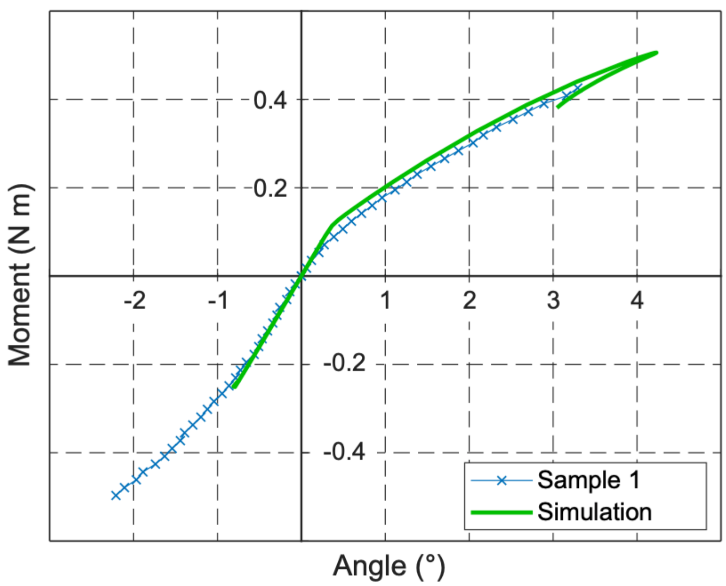

Figure 10: Comparison of simulation and experiment for sample 1 under M_X.

Figure 11 shows the moment-angle plot for bending around Y. In this case, the simulation predicts well both the pre-buckling and stable post-buckling stiffnesses. A key aspect of the numerical results is a sudden drop in both moment and rotation following the initial buckling, before transitioning to a stable post-buckling regime. This unstable region is not seen in the experimental results, as the test apparatus is not able to capture such events, but note that the buckling load from the simulation ($0.1\,\mathrm{N\,m}$) matches very well with the observed appearance of a small localized buckle during the experiment ($0.11\,\mathrm{N\,m}$). Due to multiple bifurcations encountered during the post-buckling simulation, the current numerical results do not predict the buckling collapse load as convergence is challenging at each of these bifurcations. The end of the simulation curve marks the point where convergence was no longer obtained. A different numerical technique, such as the *generalized path-following*, would be necessary to fully capture the complete post-buckling regime (Eriksson, 1998; Groh et al., 2018).

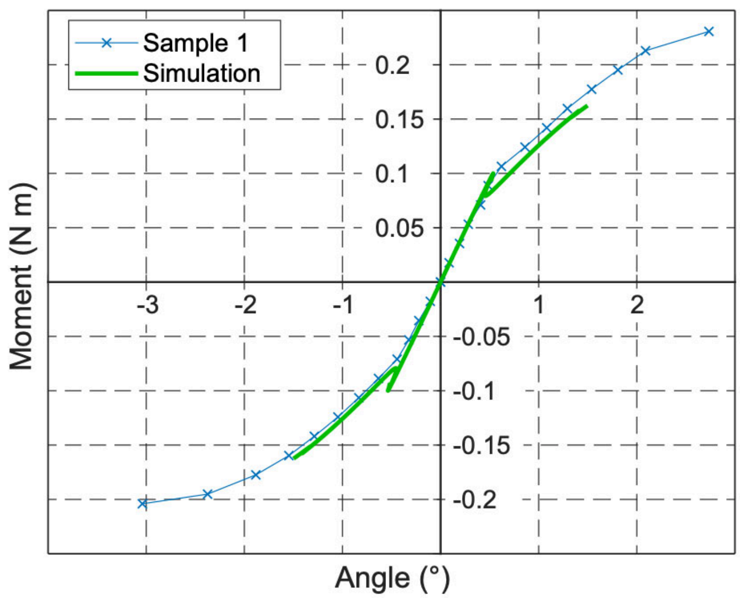

Figure 11: Comparison of simulation and experiment for sample 1 under M_Y.

5. Effect of Length on Buckling Load

The simulation framework presented in Section 3 was used to investigate the buckling behavior of TRAC booms with the nominal cross-section in Table 2 and length varying from 0.3 m to 5 m. Both linear (step 1 in Section 3) and nonlinear predictions (step 3) of buckling were obtained. The results are shown in Fig. 12 for each loading condition.

The first loading case is moments $M_X < 0$, compressing both flanges. The linear and nonlinear buckling moment predictions are plotted as a function of length in Figure 12a. From the linear prediction, two regimes are observed. For lengths smaller than 700 mm, the buckling mode is a global wave pattern with a uniform wavelength of about 52 mm for both flanges (Figure 13a.1). In this length range, the buckling load is constant with length. Increasing the length beyond 700 mm leads to a lateral-torsional buckling mode, as often found in thin-walled open cross-section beams Bazant and Cedolin (2010), (Figure 13a.2) and in this case the buckling load decreases with length. The nonlinear buckling prediction results show three regimes. For lengths up to 1000 mm the buckling mode is localized close to both ends of the boom (Figure 13b.1). For a

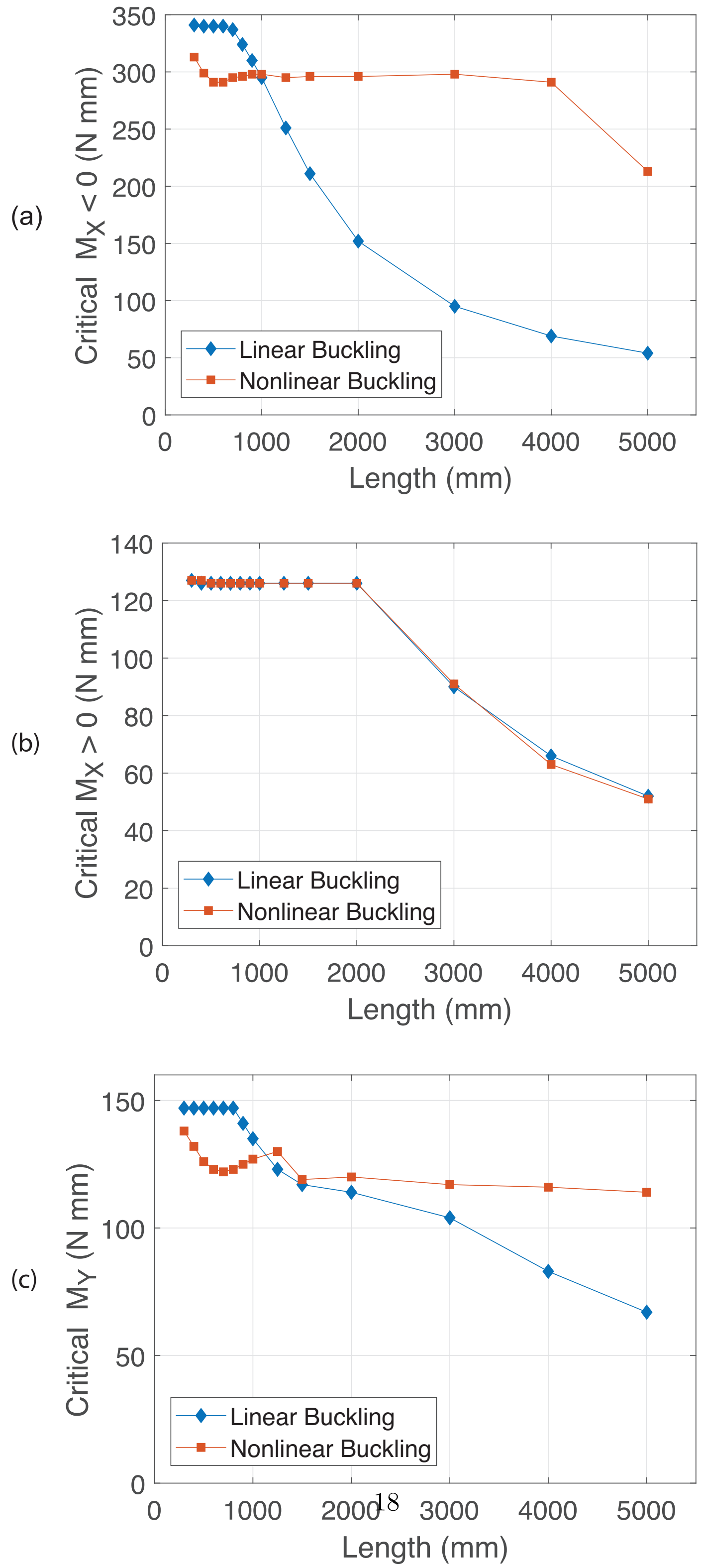

Figure 12: Critical moment as a function of boom length, both linear and nonlinear predictions, for $M_X < 0$ (a), $M_X > 0$ (b), and M_Y (c).

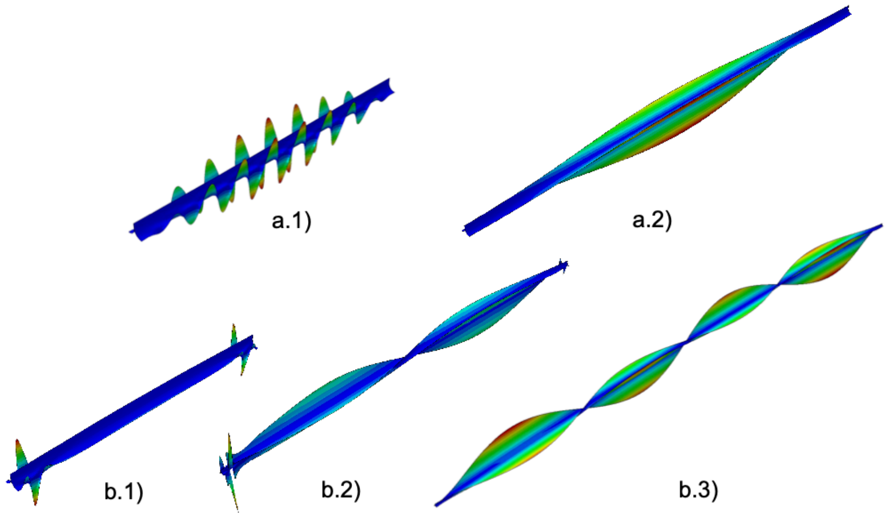

Figure 13: Buckling modes from simulation for $M_X < 0$. Linear buckling, boom length of 500 mm (a.1) and 1,250 mm (a.2). Nonlinear buckling, boom length of 500 mm (b.1), 2,000 mm (b.2) and 5,000 mm (b.3).

lengths over 5000 mm, buckling occurs with a lateral-torsional mode, but with a shorter wavelength (Figure 13b.3) than in the linear prediction. For lengths between 1000 mm and 5000 mm, the buckling mode is a combination of the two mentioned previously, as seen in Figure 13b.2. In this regime, the buckling moment is mostly constant, decreasing only by 3% when the length is increased from 1000 mm to 4000 mm.

The second loading case is moments $M_X > 0$, compressing the web. The plot of the buckling load as a function of length is shown in Figure 12b. For this loading condition, the linear and nonlinear buckling predictions practically coincide for the full range of lengths. Two regimes are observed. First, for lengths varying from 300 mm to 2000 mm, the buckling load is constant. The buckling mode (Figure 14a) is a global wave pattern with a wavelength of about 77 mm (13 half-wavelengths for a 500 mm boom), and this wavelength remains constant when the length is increased. The second regime, for lengths above 2000 mm, is once again a lateral-torsional mode (Figure 14b). However, in contrast with what was observed for moments $M_X < 0$, in this case both the linear and nonlinear results predict a single wave along the boom, with the buckling moment decreasing with length.

The last loading case is a moment M_Y. The buckling load for this case is plotted as a function of length in Figure 12c. Similarly to the other two cases, the linear prediction consists of two regimes. The critical moment is constant for lengths ranging from 300 mm to 800 mm, where the buckling mode is a wave pattern for the inner flange (Figure 15a.1), with a uniform wavelength of 45 mm that remains constant with varying length. Lateral-torsional buckling

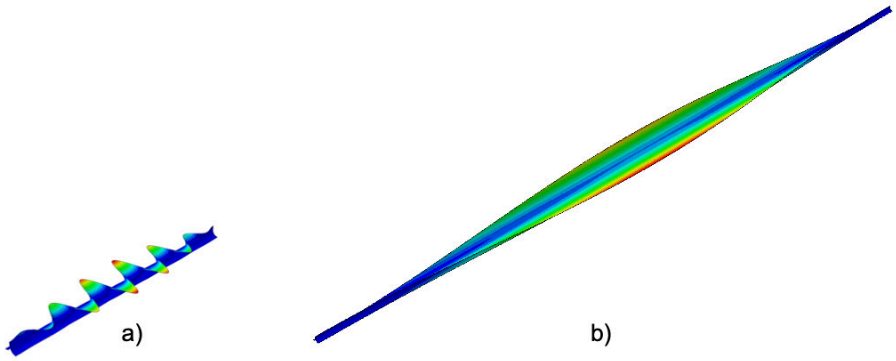

Figure 14: Buckling modes from simulation for $M_X > 0$. In this case the linear and nonlinear buckling modes are identical. (a) boom lengths of 500 mm and (b) 3,000 mm. The buckling mode in (b) is a classical lateral-torsional mode.

is observed for lengths above 800 mm (Figure 15a.2), and the critical moment decreases with length. The nonlinear buckling response is also similar to that observed for $M_X < 0$, with three regimes. First, for lengths varying from 300 mm to 1,000 mm the buckling mode is localized in the middle of the flange (Figure 15b.1) and the buckling load is relatively constant. For lengths above 2000 mm, the buckling mode is once again lateral-torsional with a shorter wavelength (3 full waves for a boom of length 3000 mm, Figure 15b.2). In the range 1,000-2,000 mm both modes are competing. The result is that the nonlinear simulation predicts an almost constant critical moment over the full range of lengths, with the buckling load decreasing by only 10% when the length increases from 1,000 mm to 5,000 mm.

While the linear buckling simulation and also the nonlinear simulation for $M_X > 0$ predict a typical buckling behavior for a thin-shell structure, with a region of constant load followed by a region where the load decreases with length, the nonlinear results for both $M_X < 0$ and M_Y of any sign are rather unexpected because the critical buckling moment remains almost constant when the length is increased.

This behavior can be explained by considering the effect of deformations that occur during the pre-buckling phase. Bending around Y will be used as an example. As shown in Figure 11, the first buckling event follows a seemingly linear phase. However, while the global structural behavior is linear in this region, large deformations occur locally in the boom. Figure 16 shows the deformation (magnified by a factor of 4) of a 3,000 mm long TRAC boom loaded by M_Y. The critical moment for this case is 117 N mm. At a moment of around 23 N mm the inner flange has already deflected down along the full length. This deformation pattern remains mostly unchanged when the moment becomes larger. For a moment of around 90 N mm there is some torsional deformation and the inner flange moves down close to the ends, but not in the middle. Finally, when the moment approaches the critical value, the torsional deformation decreases

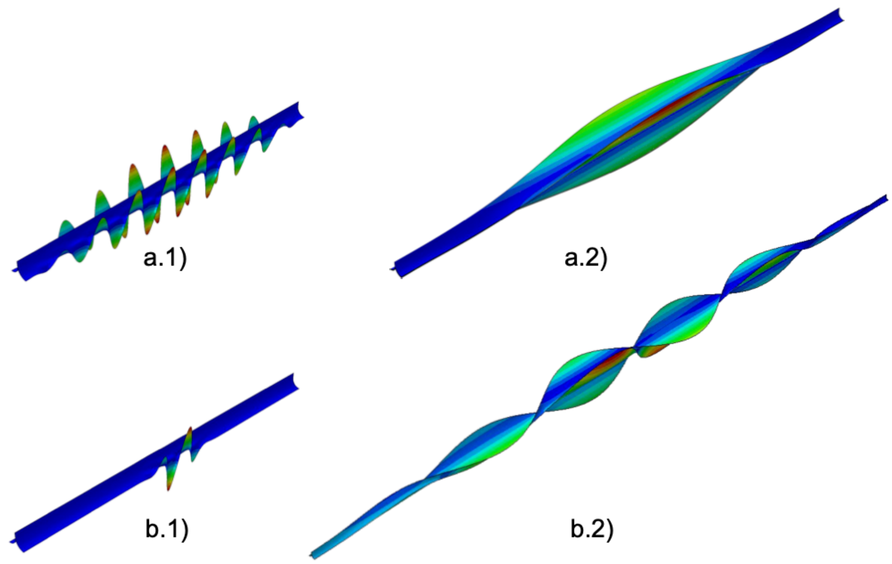

Figure 15: Buckling modes from simulation for M_Y of any sign. Linear buckling of boom with length of (a.1) 500 mm and (a.2) 1,000 mm. Nonlinear buckling of boom with length of (b.1) 500 mm and (b.2) 3,000 mm.

in wavelength, as shown in Figure 16 for an applied moment of 115 N mm. This torsional deformation prior to buckling constrains the buckling mode to a higher order lateral-torsional mode, leading to a mostly constant critical moment that is independent of the length of the boom.

6. Conclusion

This paper has investigated the buckling of ultra-thin composites TRAC booms. An in-autoclave manufacturing process was proposed, where the flanges are first cured and then bonded together in a subsequent step. The laminate used consisted of glass fiber plain weave fabric and unidirectional carbon fiber prepregs arranged symmetrically, and the stiffness properties of the laminate were measured experimentally. Three boom tests samples were built. Due to residual stresses from manufacturing, their shapes differed from the mold shape and were measured with a 3D laser scanner.

Bending of the booms was investigated experimentally by applying a pure moment around both axes of the cross-section. In both cases, a linear pre-buckling regime was observed, followed by further buckling events transitioning to a stable post-buckling regime. Buckling collapse occurred at loads up to four times higher than the initial observed buckling. For the loading cases where the flanges are in compression ($M_X < 0$ and M_Y of any sign), the first buckling event was associated with the formation of a localized buckle, which decreased the structural bending stiffness. Buckling collapse occurred when one

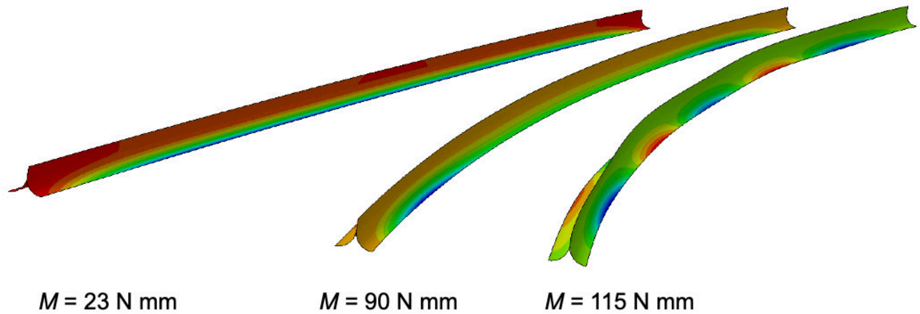

Figure 16: Nonlinear deformation in the pre-buckling regime during Y bending of a 3000 mm long boom. The color contours represent the Y displacement component, where blue is negative (down) and red is positive (up). Displacements have been magnified by a factor of 4.

flange partially flattened at the same location where the first buckle had formed, forming a kink at the intersection of the flange with the web. For $M_X > 0$, the web is under compression and the initial buckling mode is a global wave pattern of the web. This wave pattern appeared very early in the test and led to a gradual decrease of the bending stiffness. Buckling collapse occurred when the deformation localized.

A numerical simulation using the Abaqus finite-element software was used to predict the behavior of TRAC booms subjected to pure bending. The same three loading conditions were studied: $M_X < 0$ (web in tension), $M_X > 0$ (web in compression) and M_Y of any sign. In all cases, the simulation results matched closely the experimental results. The stable post-buckling regime was accurately predicted for both $M_X > 0$ and M_Y using the modified Riks method, although gradual softening near buckling collapse was not fully captured for $M_X < 0$ and M_Y.

The effect of varying the length of the booms from 300 mm to 5,000 mm was also studied numerically. When the flanges are loaded in compression ($M_X < 0$ and M_Y of any sign), nonlinearities during the pre-buckling phase have a significant effect. They lead to a length independent buckling mode across most of the length range. Hence, the critical moments for $M_X < 0$ decreased by only 3% when increasing the length from 1,000 mm to 4,000 mm, and the critical moments for M_Y of any sign decreased by only 10% when increasing the length from 1,000 mm to 5,000 mm. However, the critical moment for $M_X < 0$ and a boom length of 5,000 mm was shown to decrease significantly, suggesting that changes of behavior may occur for even longer booms. It may be interesting to further investigate this effect, if longer booms are of practical interest. When the web is loaded under compression ($M_X > 0$), both linear and nonlinear predictions agree well. After a regime with constant buckling moment, the critical load decreases with length, dropping by 60% from 2,000 mm to 5,000 mm. Knowledge of this behavior will be important for the design of TRAC booms.

Lastly, it is noted that the present study did not find significant changes in behavior between different booms with nominally identical properties and geometry. However, a systematic quantification of the stochastic behavior of booms was not carried out, and remains an open topic for further research.

Acknowledgments

Financial support from the Space Solar Power Project at the California Institute of Technology and the Natural Sciences and Engineering Research Council of Canada is gratefully acknowledged.

References

M. Aguirre-Martinez, D. Bowen, R. Davidson, R. Lee, T. Thorpe (1986), The development of a continuous manufacturing method for a deployable satellite mast in CFRP, in: British Plastics Congress, Citeseer, pp. 107–110.

M. Arya, N. Lee, S. Pellegrino (2016), Ultralight Structures for Space Solar Power Satellites, AIAA Scitech 2016 Forum, AIAA-2016-1950.

ASTM D4255/D4255M-15a (2015), Standard Test Method for In-Plane Shear Properties of Polymer Matrix Composite Materials by the Rail Shear Method, Standard, ASTM International.

J. Banik, E. Ardelean (2010), Verification of a retractable solar sail in a thermal-vacuum environment, in: 51st AIAA/ASME/ASCE/AHS/ASC Structures, Structural Dynamics, and Materials Conference 18th AIAA/ASME/AHS Adaptive Structures Conference 12th, AIAA, Orlando, FL, AIAA-2010-2585.

J. Banik, T. W. Murphey, Performance Validation of the Triangular Rollable and Collapsible Mast, in: Proceedings of the 24th Annual AIAA/USU Conference on Small Satellites, AIAA, Logan, UT.

Z. P. Bazant, L. Cedolin (2010), Stability of structures: elastic, inelastic, fracture and damage theories, World Scientific.

M. A. Bessa, S. Pellegrino (2017), Design of ultra-thin composite deployable shell structures through machine learning, in: IASS Annual Symposium "Interfaces: architecture . engineering . science", Hamburg, Germany.

B. Betts, D. Spencer, B. Nye, R. Munakata, J. M. Bellardo, S. D. Wong, A. Diaz, R. W. Ridenoure, B. A. Plante, J. D. Foley, et al. (2017), Lightsail 2: Controlled solar sailing using a CubeSat, in: The 4th International Symposium on Solar Sailing. Kyoto Research Park, Kyoto, Japan.

C. Biddy, T. Svitek (2012), LightSail-1 solar sail design and qualification, in: Proceedings of 41st Aerospace Mechanisms Symposium, Pasadena, CA.

D. Campbell, R. Barrett, M. S. Lake, L. Adams, E. Abramson, M. Scherbarthn, J. S. Welsh, G. Freebury, N. Beidleman, J. Abbot (2006), Development of a novel, passively deployed roll-out solar array, in: 2006 IEEE Aerospace Conference, IEEE.

E. Corona, M.S. Ellison (1997), Plastic buckling of T-beams under pure bending, Journal of Engineering Mechanics 123, 466-474.

K. Cox, K. A. Medina (2019), Scalability of Triangular Rollable and Collapsible Booms. AIAA Scitech 2019 Forum, AIAA-2019-2026.

M. A. Crisfield (1981), A fast incremental/iterative solution procedure that handles snap-through, in: A. K. Noor, H. G. McComb (Eds.), Computational Methods in Nonlinear Structural and Solid Mechanics, Pergamon, pp. 55 – 62.

I. M. Daniel, O. Ishai (2005), Engineering mechanics of composite materials, 2nd edition Oxford University Press, New York.

A. Eriksson (1988), Structural instability analyses based on generalised path-following, Computer Methods in Applied Mechanics and Engineering 156, 45 – 74.

J. M. Fernandez (2017), Advanced Deployable Shell-Based Composite Booms for Small Satellite Structural Applications Including Solar Sails, in: 4th International Symposium on Solar Sailing, Tokyo, Japan.

J. M. Fernandez (2018), Sheath-based rollable lenticular-shaped and low-stiction composite boom, US Patent 9,863,148.

R. Groh, D. Avitabile, A. Pirrera (2018), Generalised path-following for well-behaved nonlinear structures, Computer Methods in Applied Mechanics and Engineering 331, 394 – 426.

L. Herbeck, M. Leipold, C. Sickinger, M. Eiden, W. Unckenbold (2001), Development and test of deployable ultra-lightweight cfrp-booms for a solar sail, in: Spacecraft Structures, Materials and Mechanical Testing, volume 468, p. 107.

B. Hoang, S. White, B. Spence, S. Kiefer (2016), Commercialization of Deployable Space Systems' roll-out solar array (ROSA) technology for Space Systems Loral (SSL) solar arrays, in: 2016 IEEE Aerospace Conference, IEEE, pp. 1–12.

L. Johnson, M. Whorton, A. Heaton, R. Pinson, G. Laue, C. Adams (2011), NanoSail-D: A solar sail demonstration mission, Acta Astronautica 68, 571–575.

C. Leclerc, L. Wilson, M. A. Bessa, S. Pellegrino (2017), Characterization of Ultra-Thin Composite Triangular Rollable and Collapsible Booms, in: 2017 AIAA SciTech Forum, Grapevine, TX, AIAA-2017-0172.

C. Leclerc, A. Pedivellano, S. Pellegrino (2018), Stress Concentration and Material Failure during Coiling of Ultra-Thin TRAC Booms, in: 2018 AIAA SciTech Forum, AIAA-2018-0690.

C. Leclerc, S. Pellegrino (2019), Reducing Stress Concentration in the Transition Region of Coilable Ultra-Thin-Shell Booms, in: 2019 AIAA SciTech Forum, AIAA-2019-1522.

M. Leipold, M. Eiden, C. Garner, L. Herbeck, D. Kassing, T. Niederstadt, T. Krüger, G. Pagel, M. Rezazad, H. Rozemeijer, W. Seboldt, C. Schöppinger, C. Sickinger, W. Unckenbold (2003), Solar sail technology development and demonstration, Acta Astronautica 52 317 – 326. Selected Proceedings of the 4th IAA International conference on Low Cost Planetary Missions.

M. Leipold, H. Runge, C. Sickinger (2005), Large SAR membrane antennas with lightweight deployable booms, in: 28th ESA Antenna Workshop on Space Antenna Systems and Technologies, , ESA/ESTEC, Noordwijk, The Netherlands, p. 8.

T. W. Murphey, J. Banik, Triangular rollable and collapsible boom, . US Patent 7,895,795.

T. W. Murphey, D. Turse, L. Adams 2011, TRAC Boom Structural Mechanics, in: 4th AIAA Spacecraft Structures Conference, Grapevine, TX.

X. Ning, S. Pellegrino (2017), Experiments on imperfection insensitive axially loaded cylindrical shells, International Journal of Solids and Structures 115-116, 73 – 86.

E. Pollard, T. Murphey (2006), Development of Deployable Elastic Composite Shape Memory Alloy Reinforced (DECSMAR) Structures. In 47th AIAA/ASME/ASCE/AHS/ASC Structures, Structural Dynamics, and Materials Conference, AIAA-2006-1681.

F. P. J. Rimrott (1965), Storable tubular extendible member: a unique machine element, Machine Design 37, 156–165.

F. Roybal, J. Banik, T. Murphey (2007), Development of an elastically deployable boom for tensioned planar structures, in: 48th AIAA/ASME/ASCE/AHS/ASC Structures, Structural Dynamics, and Materials Conference, AIAA-2007-1838.

M. Sakovsky, S. Pellegrino (2019), Closed cross-section dual-matrix composite hinge for deployable structures, Composite Structures 208 784 – 795.

O. R. Stohlman, E. R. Loper (2016), Thermal deformation of very slender triangular rollable and collapsible booms, in: 3rd AIAA Spacecraft Structures Conference, San Diego, California, AIAA-2016-1469.

M. Whorton, A. Heaton, R. Pinson, G. Laue, C. Adams (2008), Nanosail-D: the first flight demonstration of solar sails for nanosatellites, 22nd AIAA/USU Conference on Small Satellites.